

A Large-scale Finite Element Model on Micromechanical Damage and Failure of Carbon Fiber/Epoxy Composites Including Thermal Residual Stress

P. F. Liu^{1,2,3} · X. K. Li¹

Received: 15 July 2017 / Accepted: 28 July 2017 / Published online: 9 September 2017
© Springer Science+Business Media B.V. 2017

Abstract The purpose of this paper is to study micromechanical progressive failure properties of carbon fiber/epoxy composites with thermal residual stress by finite element analysis (FEA). Composite microstructures with hexagonal fiber distribution are used for the representative volume element (RVE), where an initial fiber breakage is assumed. Fiber breakage with random fiber strength is predicted using Monte Carlo simulation, progressive matrix damage is predicted by proposing a continuum damage mechanics model and interface failure is simulated using Xu and Needleman's cohesive model. Temperature dependent thermal expansion coefficients for epoxy matrix are used. FEA by developing numerical codes using ANSYS finite element software is divided into two steps: 1. Thermal residual stresses due to mismatch between fiber and matrix are calculated; 2. Longitudinal tensile load is further exerted on the RVE to perform progressive failure analysis of carbon fiber/epoxy composites. Numerical convergence is solved by introducing the viscous damping effect properly. The extended Mori-Tanaka method that considers interface debonding is used to get homogenized mechanical responses of composites. Three main results by FEA are obtained: 1. the real-time matrix cracking, fiber breakage and interface debonding with increasing tensile strain is simulated. 2. the stress concentration coefficients on neighbouring fibers near the initial broken fiber and the axial fiber stress distribution along the broken fiber are predicted, compared with the results using the global and local load-sharing models based on the shear-lag theory. 3. the tensile strength of composite by FEA is compared with those by the shear-lag theory and experiments.

✉ P. F. Liu
pfliu@zju.edu.cn; 56691747@qq.com

¹ Institute of Chemical Machinery and Process Equipment, School of Energy Engineering, Zhejiang University, Hangzhou 310027, China

² State Key Laboratory of Mechanics and Control of Mechanical Structures, Nanjing University of Aeronautics and Astronautics, Nanjing 210016, China

³ State Key Laboratory of Strength and Vibration of Mechanical Structures, Xi'an Jiaotong University, Xi'an 710049, China

Finally, the tensile stress-strain curve of composites by FEA is applied to the progressive failure analysis of composite pressure vessel.

Keywords Micromechanical progressive failure · Matrix cracking · Interface stress transfer and interface debonding · Fiber breakage · Carbon fiber/epoxy composites · Finite element analysis (FEA)

1 Introduction

It is widely recognized progressive damage and failure properties of lightweight composites are essentially multiscale ranging from microscopic to macroscopic scales, which are involved in such as fiber breakage, matrix cracking and interface failure. Moreover, there complicated micromechanical failure mechanisms evolve and interact, leading to macroscopic performance degradation and ultimate failure of composites. In order to predict the damage tolerance and load-bearing ability of composite structures, an ultimate strategy is to perform multiscale analysis by developing advanced theory and numerical technique [1].

In general, comprehensive research on the damage and failure of composites should consider the fiber/matrix/interface phases integrately. An initial matrix crack due to defects nucleates, propagates and reaches the interface, leading to the fiber bridging effect for fiber-reinforced composites. Once the fiber bridging stress exceeds the fiber strength, quasi-brittle fiber breakage results in the load redistribution and excessive load-bearing on neighbouring fiber and matrix near the broken fiber. At small scale, the conventional shear-lag theory [2] analyzes the interface stress transfer and interface fracture properties well by establishing the relationship between the interface frictional stress and the fiber tensile stress. Later, many scholars [3–9] further studied the single fiber and multiple fiber/matrix interface stress transfer with elastic and elastic-plastic matrix using the shear-lag theory although it neglected some factors such as the Poisson's effect and the fiber and matrix shear, radial and hoop stresses. No matter from theory and experiment, fiber pull-out becomes an effective approach to test the interface bonding properties of composites [10–12], where the stress-based and energy release rate-based interface fracture criteria are widely adopted. As an extension over the shear-lag theory, the Green's function-based method [13, 14] was also proposed to predict the damage evolution and tensile strength of large-scale composite models with multiple fibers. A central feature for these advanced theories is to emphasize the effect of multiple fiber breakage on the stress concentration, interface stress transfer and statistical tensile strength of composites.

For non-homogenized composites, the stress concentration and strain localization phenomena due to broken fibers inevitably aggravate the damage and failure of different phases [15, 16]. Currently, two types of load-sharing models based on the shear-lag theory were developed to describe the stress redistributions after fiber breakage: the global load-sharing (GLS) model [17] and the local load-sharing (LLS) model [18]. Landis et al. [19] showed the failure of composites can fall between the extremes of GLS and nearest neighbouring LLS. GLS is associated with the material where fiber breakage does not cause distinct stress concentrations in neighbouring fiber and the stress along a broken fiber recovers to the applied stress linearly from the break. In contrast, LLS assumes that intact fiber experiences a stress concentration in the presence of a fiber break. Although these models achieved large success at different scales to a large extent, there are still some defects for LLS since it does not accurately describe the extent of load redistribution and the influence of some micromechanical parameters.

With the increase of computer ability, finite element analysis (FEA) has become a powerful tool to predict the multiscale damage and failure behaviors of large-scale composite structures. Xia et al. [20] showed it is insufficient to focus only on the single fiber breakage problem and myriad detail associated with it. In large-scale analysis on the representative volume element (RVE), all details from the local micromechanical fiber/matrix/interface failure to the macroscopic damage evolution of composite structures are expected to be evaluated appropriately. Many scholars have performed FEA by micromechanical modeling to predict progressive failure properties of composites [21–24], but little work concentrates on the longitudinal progressive failure analysis of large-scale composite structures by 3D FEA. In FEA by Xia et al. [13, 20], zero interface bonding strength and completely debonded frictional interface were assumed by considering thermal residual stress for SiC fiber/metal matrix composites, but may not be this case for carbon fiber/epoxy composites with much lower processing temperature. Essentially, it is beyond doubt complete failure characteristics of different phases should be considered in multiscale FEA, particularly in the presence of thermal residual stress.

Liu et al. [25] developed a set of theoretical model and numerical technique to predict micromechanical damage and failure behaviors of small-scale composite models with square fiber distribution. In this research, these methods are further employed to predict the damage and failure behaviors of large-scale composite models, in which RVE with hexagonal fiber distribution is established for FEA. It is noted the hexagonal cell model describes more precise load transfer and stress concentration behaviors than the square cell model. Fiber breakage with random fiber strength is predicted using Monte Carlo simulation, progressive matrix cracking is predicted by proposing a continuum damage mechanics model and interface failure is simulated using Xu and Needleman's cohesive model. Numerical results are presented in terms of the stress concentration, progressive damage behaviors and tensile strengths of composite model. The developed numerical technique helps to gain deeper insight into the multiscale failure mechanisms and the strength prediction of composite pressure vessel and other composite structures.

2 Micromechanical Damage Modeling and FEA on the RVE

2.1 Finite Element Model of the RVE

According to microscopic observation of composites, two relatively regular fiber distributions in the matrix for T700/epoxy composites exist: square and hexagonal distributions [26]. In this work, the hexagonal RVE for large-scale micromechanical model is established for the failure analysis. The fiber radius is $R_f = 3.5\text{e-}3$ mm, the fiber volume fraction is 62% and the axial length is $L = 80\text{e-}3$ mm. FEA of the RVE is performed with ANSYS-APDL (ANSYS PARAMETRIC DESIGN LANGUAGE). 3D eight-node Solid45 element is used to mesh the fiber and matrix. Fiber breakage is simulated using the Weibull distribution, the zero-thickness Inter205 element using the Xu and Needleman's interface cohesive model [27] is employed to simulate the crack initiation and propagation of the fiber/matrix interface. In order to capture the stress concentration accurately, the mesh is refined at the initial broken fiber. The finite element model is shown in Fig. 1. The axial length $\Delta z = L/20 = 4\text{e-}3$ mm of each element is selected. The number of fiber and matrix is 11,360 and 4480, respectively.

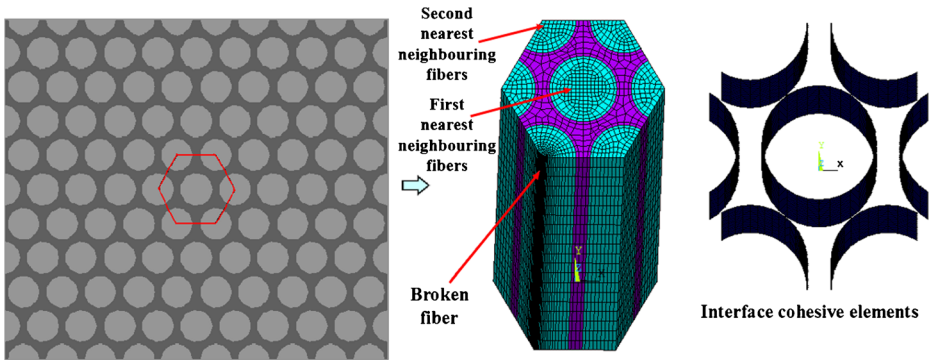


Fig. 1 The finite element model for the hexagonal RVE

2.2 Failure Criteria and Damage Models of the RVE

2.2.1 Failure criterion and strength distributions for carbon fiber

Fiber is considered as transversely isotropic and quasi-brittle. The maximum stress failure criterion for fiber is assumed as

$$|\sigma_{fz}| < X_f \tag{1}$$

where X_f is the statistical tensile strength obeying the Weibull distributions.

Similar to Li [28], the strength distribution of each fiber element is written by the two-parameter Weibull function

$$F(\sigma_f) = 1 - \exp \left[-\frac{\Delta z}{L_0} \left(\frac{\sigma_{fz}}{\sigma_0} \right)^m \right] \tag{2}$$

where F is the failure probability of fiber element at a stress level equal to or smaller than the axial fiber stress σ_f , m is the shape parameter that characterizes the flaw size distributions and σ_0 is the scale parameter at a gauge length L_0 that describes the characteristic strength of fibers. After a random number η within the interval $[0,1]$ is selected, the tensile strength X_f of each fiber element is obtained

$$X_f = \sigma_0 \left[-\frac{L_0}{\Delta z} \ln(1-\eta) \right]^{1/m} \tag{3}$$

where $m = 12.06$ is Weibull modulus, $L_0=8$ mm and $\sigma_0=4.41$ e3GPa for T700 fiber based on the fiber bundles theory and statistical theory [29].

2.2.2 Failure criterion and damage modeling for epoxy matrix

In the conventional shear-lag model [3–9], the epoxy matrix is considered to be linear elastic without damage and failure. In this work, the initial damage and progressive failure are introduced for epoxy matrix.

By considering the hydrostatic effect, Ha *et al.* [30] proposed a modified Mises failure criterion

$$\left(\frac{\sigma_{eq}}{\sigma_{eq}^{cr}}\right)^2 + \frac{J_1}{J_1^{cr}} = 1 \tag{4}$$

where $\sigma_{eq} = \sqrt{\frac{3}{2}\mathbf{S}:\mathbf{S}}$ is the Mises effective stress, $J_1 = tr(\boldsymbol{\sigma})$ is the first stress invariant and $\mathbf{S} = \boldsymbol{\sigma} - tr(\boldsymbol{\sigma})/3I_2$ is the deviatoric stress tensor and I_2 is the two-order unit tensor. $\sigma_{eq}^{cr} = \sqrt{T_m C_m}$ and $J_1^{cr} = C_m T_m / (C_m - T_m)$ are critical values. $C_m = 120\text{MPa}$ and $T_m = 80\text{MPa}$ are the compressive and tensile strengths of the epoxy matrix, respectively.

Liu *et al.* [25] developed a continuum damage mechanics-based model for isotropic epoxy. The relationship between the effective elastic tensor $\bar{\mathbf{C}}$ and the nominal tensor \mathbf{C} is given by

$$\bar{\mathbf{C}} = \mathbf{C} / (1-d), \quad \mathbf{C} = \lambda I_2 \otimes I_2 + 2\mu I_4 \tag{5}$$

where d is the damage variable, I_4 is the four-order unit tensor. λ and μ are Lamé constants.

The damage variable d is written as [25]

$$d = 1 - \exp(-Y / Y_c) \tag{6}$$

where Y_c is the critical value of the thermal conjugate force Y that is given by Lemaitre and Desmorat [31]

$$Y = \frac{\sigma_{eq}}{2E_m} \left[\frac{2}{3} (1 + \nu_m) + 3(1 - 2\nu_m) \left(\frac{tr(\boldsymbol{\sigma})}{3\sigma_{eq}} \right) \right] \tag{7}$$

where E_m and ν_m are the Young’s modulus and Poisson’s ratio of epoxy. From Eqs.(6) and (7), the damage variable d is obtained.

2.2.3 Exponential cohesive model for interface debonding

Xu and Needleman’s exponential cohesive model [27] is used, as shown in Fig. 2a. The surface potential function $\phi(\delta)$ is given by

$$\begin{cases} \phi(\delta) = e\sigma_{\max}\bar{\delta}_n \left[1 - (1 + \Delta_n)e^{-\Delta_n} e^{-\Delta_t^2} \right] \\ T_n = e\sigma_{\max}\Delta_n e^{-\Delta_n} e^{-\Delta_t^2} \\ T_t = 2e\sigma_{\max}\frac{\bar{\delta}_n}{\delta_t}\Delta_t(1 + \Delta_n)e^{-\Delta_n} e^{-\Delta_t^2} \\ \Delta_n = \frac{\delta_n}{\bar{\delta}_n}, \quad \Delta_t = \frac{\delta_t}{\bar{\delta}_t} \end{cases} \tag{8}$$

where T_n and T_t are the normal and tangential tractions, respectively. Δ_n and Δ_t are the normalized normal and tangential opening displacements, respectively. σ_{\max} and $\bar{\delta}$ are the maximum traction and the corresponding displacement jump at that point, respectively. Cohesive model is implemented using middle-plane interpolation technique, as shown in Fig. 2b.

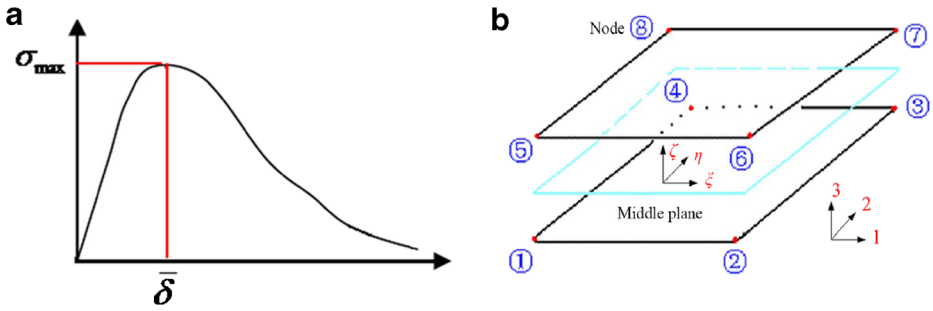


Fig. 2 (a) Xu and Needleman’s exponential cohesive model and (b) Middle-plane relative-displacement interpolation technique for cohesive model

After interface debonding, the debonded interface may contact with friction. From micromechanical damage and failure analysis of metal matrix composites, Xia et al. [13, 20] showed the composite tensile strength is rather insensitive to the friction coefficient. Thus, the frictional contact of the debonded interface is not considered in this work.

2.3 Mori-Tanaka Homogenization Method for Composite with Interface Debonding

Hori and Nemat-Nasser [32] pointed out the fundamental assumption of the mean-field homogenization method is that the strain and stress are piecewise uniform in each phase in an RVE. The volume average of the strain ϵ and stress σ for fiber and matrix is given by respectively

$$\langle \epsilon \rangle^p = \frac{1}{V^p} \int_{V^p} \epsilon dV, \quad \langle \sigma \rangle^p = \frac{1}{V^p} \int_{V^p} \sigma dV, \quad (p = f, m) \tag{9}$$

where V is the volume.

The conventional Mori-Tanaka method does not consider the effect of interface debonding. Hori and Nemat-Nasser [32] showed the macroscopic strain must introduce an additional strain due to interface failure. For composites with interface debonding, the average macroscopic stress $\langle \sigma \rangle$ and strain $\langle \epsilon \rangle$ are written as [33]

$$\begin{cases} \langle \sigma \rangle = f \langle \sigma \rangle^f + (1-f) \langle \sigma \rangle^m, \\ \langle \epsilon \rangle = f \langle \epsilon \rangle^f + (1-f) \langle \epsilon \rangle^m + f \langle \epsilon \rangle^{\text{int}}, \\ \langle \epsilon \rangle^{\text{int}} = \frac{1}{2V^f} \int_{s^{\text{int}}} ([\mathbf{u}] \times \mathbf{n} + \mathbf{n} \times [\mathbf{u}]) dA, \quad [\mathbf{u}] = \mathbf{u}^m - \mathbf{u}^f \end{cases} \tag{10}$$

where f is the fiber volume fraction. $\langle \epsilon \rangle^{\text{int}}$ is the superimposed strain due to interface debonding. s^{int} denotes the discontinuous interface. \mathbf{n} is the unit normal vector on the interface pointing to the matrix. \mathbf{u}^m and \mathbf{u}^f are the displacements on the interface from the matrix side to the fiber side, respectively. V^f is the fiber volume in the RVE.

The strain concentration factors \mathbf{B}^ϵ and \mathbf{A}^ϵ are defined as follows

$$\langle \epsilon \rangle^f = \mathbf{B}^\epsilon : \langle \epsilon \rangle^m = \mathbf{A}^\epsilon : \langle \epsilon \rangle = \mathbf{A}^\epsilon : [f \langle \epsilon \rangle^f + (1-f) \langle \epsilon \rangle^m + f \langle \epsilon \rangle^{\text{int}}] \tag{11}$$

Liu et al. [25] performed multiscale analysis of composite structures using the asymptotic homogenization method that involves the interaction between the macroscopic and

microscopic data. However, this requires a huge amount of computational resources for large composite structures. By comparison, the Mori-Tanaka mean-field method is easier to implement by FEA and requires several orders of magnitude smaller computational time.

2.4 Material Parameters and Finite Element Analysis

The Young’s modulus E_f and Poisson’s ratio ν_f for T700 fiber are 227GPa and 0.3, respectively. The longitudinal and transverse thermal expansion coefficients α_f for T700 fiber are $-0.52 \times 10^{-6}/^\circ C$ and $10 \times 10^{-6}/^\circ C$, respectively [25]. $Y_c = 1000\text{MPa}$ in Eq.(6) is used. The cohesive interface parameters in Eq.(8) are taken as $\sigma_{\max} = 75\text{MPa}$ and $\bar{\delta}_n = \bar{\delta}_t = 2\text{E-}4\text{mm}$, respectively. The Poisson’s ratio ν_m of epoxy is 0.4. Experiments showed that the Young’s modulus and thermal expansion coefficient of epoxy depend on temperature largely. The Young’s modulus $E_m(T)$ of epoxy can be written by three expressions [34]

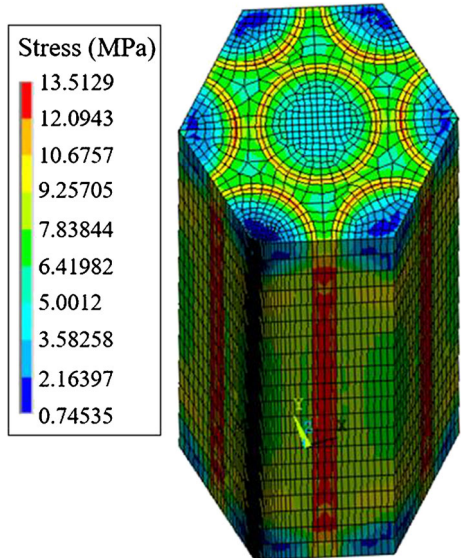
$$\begin{aligned}
 \text{(a) } E_m(T) &= E_m(T_g - \Delta T_1) \exp\left(-k_2 \frac{T - T_g + \Delta T_1}{\Delta T_1 + \Delta T_2}\right), & T_g - \Delta T_1 \leq T \leq T_g + \Delta T_2, \\
 \text{(b) } E_m(T) &= E_m(T_r) \exp\left(-k_1 \frac{T - T_r}{T_g - \Delta T_1 + T_r}\right), & T \leq T_g - \Delta T_1, \\
 \text{(c) } E_m(T) &= 0.01 \times E_m(T_r), & T \geq T_g + \Delta T_2
 \end{aligned}
 \tag{12}$$

The thermal expansion coefficient α_m of epoxy is assumed to vary linearly with temperature and the slope is written as [34]

$$k = \frac{\alpha_1 - \alpha_m(T_r)}{T_g - T_r}
 \tag{13}$$

where the glassy transition temperature $T_g = 110^\circ C$, $T_r = 23^\circ C$, $\Delta T_1 = \Delta T_2 = 35^\circ C$, $E_m(T_r) = 3.35\text{GPa}$, $E_m(T_r - \Delta T_1) = 0.7E_m(T_r)$, $E_m(T_r + \Delta T_2) = 0.01E_m(T_r)$, $k_1 = 0.35667$, $k_2 = 4.2485$, $\alpha_m(T_r) = 58 \times 10^{-6}/^\circ C$, $\alpha_1 = 139 \times 10^{-6}/^\circ C$.

Fig. 3 The distributions of thermal residual stress (Mises stress) of RVE after curing



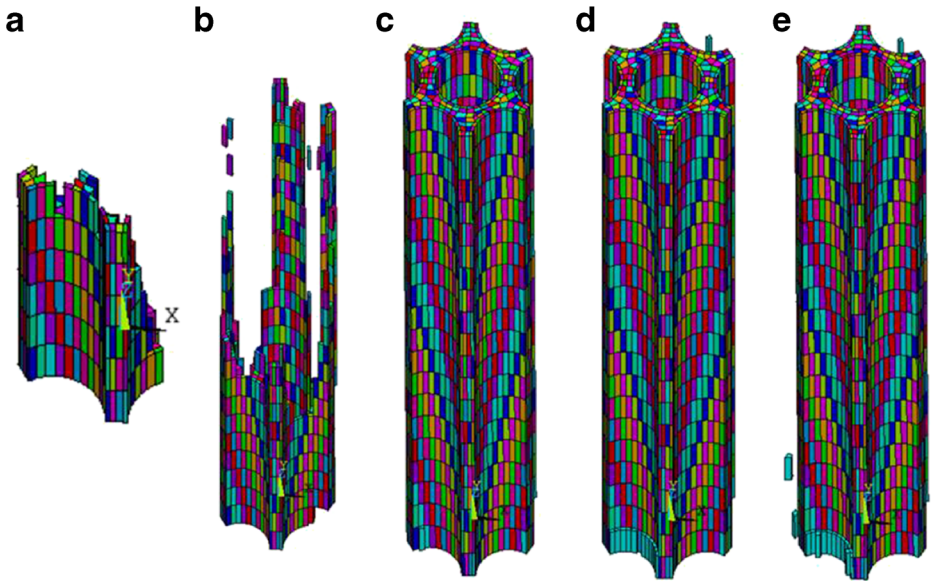


Fig. 4 The progressive damage evolution processes for fiber and matrix elements at the tensile strains (a) 1%, (b) 1.125%, (c) 1.25%, (d) 1.75% and (e) 2.125% respectively

Progressive failure analysis of the RVE is implemented using ANSYS-APDL (ANSYS Parametric Design Language). FEA is divided into two steps: 1. periodic boundary conditions [35] are exerted on all opposite sides of the RVE for calculating the thermal residual stress from curing temperature of epoxy 149 °C to room temperature 20 °C, in which discrete thermal expansion coefficients with temperature are used. In addition, all constraints are exerted on any one selected node to eliminate the rigid displacement. 2. periodic boundary conditions for the broken fiber surface are removed and the axial tensile load is applied on the opposite surfaces at room temperature. The restart analysis is used to update the degraded material parameters of fiber and matrix after each load increment and the viscous stabilization method is used to solve the numerical convergence problem at the strength limit of the RVE.

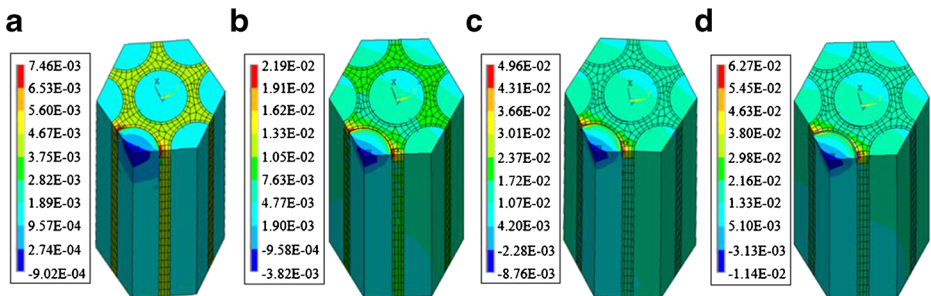


Fig. 5 The interface debonding process at the tensile strains (a) 0.25%, (b) 0.625%, (c) 1.25% and (d) 1.875%

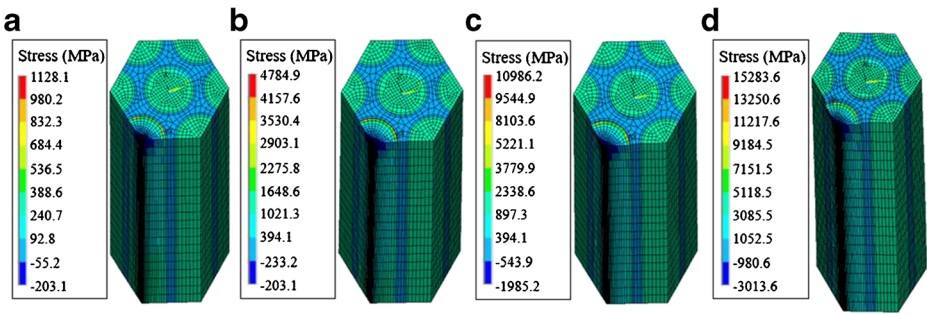


Fig. 6 The axial stresses on fiber and matrix elements at the tensile strains (a) 0.25%, (b) 0.625%, (c) 1.25% and (d) 1.875% respectively

3 Numerical Results and Discussion

Figure 3 shows the distributions of thermal residual stress after curing. Since the temperature dependent thermal expansion coefficients of epoxy are higher than those of fiber, thermal residual stress occurs mainly at the epoxy. However, the thermal stress does not lead to the initial failure of matrix. Figure 4 shows the progressive damage evolution process for fiber and matrix elements. Figure 5 shows the interface debonding process. At about the strain 0.5%, the RVE starts to fail in the form of matrix cracking with 6 failed matrix elements, which appears at near the initial broken fiber. The fiber/matrix interface starts to debond near the broken fiber at about the strain 0.625%, accompanied by 16 failed matrix elements. At the strain 1.125%, there are 1137 failed matrix elements. Fiber breakage starts to appear at the strain 1.25% and at this time all matrix elements (4480) have failed and more severe interface debonding appears. At the strain 2.125%, 26 fiber elements and 4480 matrix elements fail, indicating complete damage of the RVE. It is noted the initial broken fiber induces the accumulation of failed fiber, matrix and interface elements, which accelerates the localized damage of RVE. The

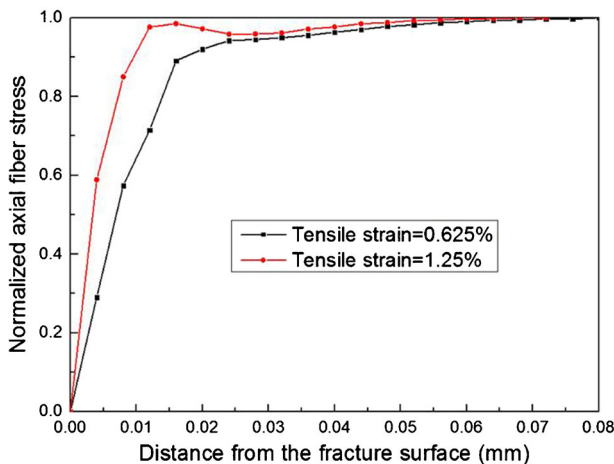


Fig. 7 The axial fiber stress distributions on the broken fiber from the fracture surface at the tensile strains 0.625% and 1.25% respectively

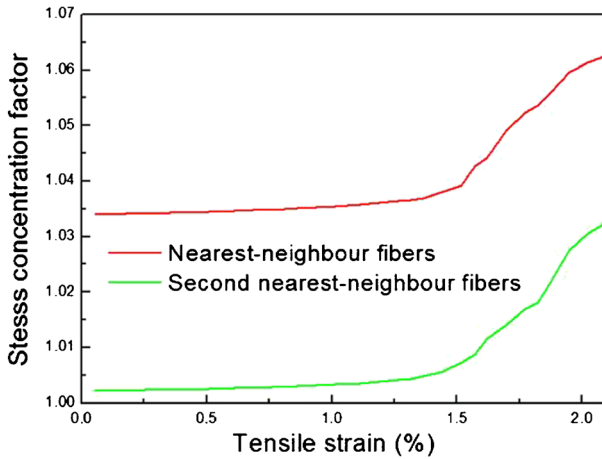


Fig. 8 The axial stress concentration factor $k(z)$ of neighbouring fibers around the initial broken fiber with the increase of tensile strain

progressive failure properties of the RVE can be compared with the acoustic emission (AE) test results on T700 fiber/epoxy composites under tension [25]. AE is mainly represented by the amplitude parameters reflecting the signal strength of different failure modes. The damage evolution process of composites is divided into three stages: (a) At the early stage (0–200 s), the matrix cracking with the 50–60 dB amplitude other than fiber fracture appears. (b) At the middle damage stage (200–1000s), the dominating failure modes are still matrix cracking, accompanied by very little fiber breakage with beyond 80 dB amplitude. (c) At the stage of fracture (1000–1200s), the number of fiber fracture adds, indicating the ultimate collapse of specimen. Experimental results are consistent with numerical analysis.

The initial broken fiber introduces the stress redistribution and localized damage on neighbouring fibers. Figure 6 shows the axial stresses on fiber and matrix elements at different strains. It is noted severe stress concentration appears the broken fiber and neighbouring matrix, and gradually extends to neighbouring fibers. Since the cohesive model belongs to a phenomenological model, true interface shear and normal stresses are not given here. Figure 7 shows the axial stress distributions on the broken fiber from the fracture surface (normalized by the far-field fiber stress σ_∞ and averaged over the fiber cross-section) at the tensile strains 0.625% and 1.25% respectively. The axial fiber stress first recovers gradually from zero at the fracture surface to the smooth far-field fiber stress and then remains constant. Xia et al. [13, 20] showed the slip length l_s for the initially debonded interface (or called as the stress recovery length or inefficient load transfer length for initially bonded interface) can be evaluated by the formula $l_s = r_f \sigma_\infty / 2\tau$ using the simple shear-lag model and constant interface friction stress τ . If

Table 1 Stress concentration factor (SCF) at the tensile strain 1.25%

	Square RVE [25]	Hexagonal RVE [18]	GLS model [17]	LLS model
1	1.085	1.035	1.0011	1.1046
2	1.055	1.002	1.0011	1.0100

where ‘1’ and ‘2’ represent the first and second nearest-neighbouring fibers around the broken fiber



Fig. 9 The tensile experiments of unidirectional carbon fiber/epoxy composite specimens

the frictional stress is replaced by the cohesive traction, the analytical l_s is about 0.02 mm at the tensile strain 0.625%, close to the numerical solution in Fig. 7. However, the numerical result for the slip length is larger than the analytical solution when the strain continues to increase.

Figure 8 shows the axial stress concentration factor $k(z)$ (SCF, the local axial fiber stress normalized by the far-field fiber stress $\sigma_{f_{\infty}}$ and averaged over the fiber cross-section) of neighbouring fibers around the broken fiber. The SCF adds slightly with the increase of tensile strain. More stresses are redistributed on the first nearest-neighbouring fibers than those on the second and third nearest-neighbouring fibers. By comparison, the analytical solutions using the global load-sharing (GLS) model [17] and the local load-sharing (LLS) model [18] are also provided. The GLS model assumed all intact fibers share the applied loads equally and thus equally carry the loads lost from broken fibers, where sufficiently low interfacial shear stress is assumed. In the LLS model, only the immediate unbroken neighbouring fibers carry these lost loads, thereby causing more severe overloads than those that appear by the GLS model. The LLS model considered a fiber composite consisting of infinite hexagonally aligned fibers embedded in the elastic matrix and is more accurate than the GLS model because it accounts for the effects of the elastic deformations of the fiber and matrix on the redistribution of tensile

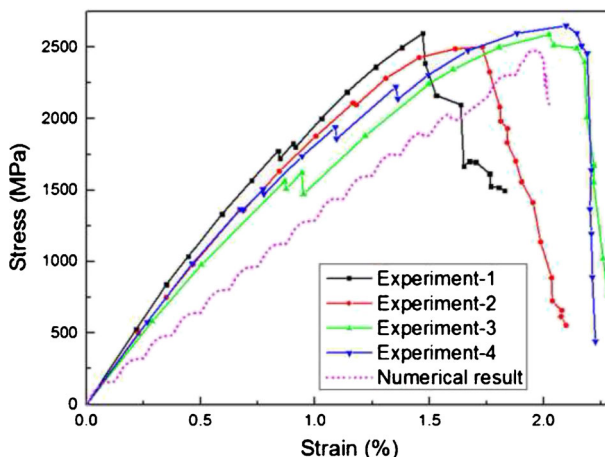


Fig. 10 The tensile stress-strain curves of composites by FEA and experiments

Table 2 Composite tensile strengths, as predicted and measured

	Hexagonal RVE	Curtin's model [13, 14, 17, 18, 20] $\tau = 20 - 120\text{MPa}$	Experiments (Average value)
UTS(MPa)	2475	2256–2586	2585

stress based on the shear-lag theory. Further, the modified shear-lag model [13, 14] considered the geometry of finite periodic patches based on the shear-lag model and applied an influence function technique to solve a 3D stress field around the broken fiber. Table 1 compares the SCFs obtained by FEA and analytical models. The SCFs obtained by the GLS model are the smallest among all models. The GLS model decreases the stress concentration around the broken fiber and underestimates the sharing portions of the loads borne by the neighbouring intact fibers. For the second-neighbouring fibers, the SCF obtained by the RVE is basically consistent with that by the LLS, but large difference appears for the first nearest-neighbouring fibers. This can be interpreted as: the LLS model neglects the matrix tensile stress and assumes the matrix to be in a state of only pure elastic shear. Therefore, the first nearest-neighbouring fibers bears more stresses in the LLS. In addition, Blassiau et al. [26] compared the SCF using the square and hexagonal cell models of for carbon fiber/epoxy composites with initially bonded and debonded interface. They considered the elastic matrix without damage evolution and used the interface node bonding technique to simulate the interface debonding. From the present FEA, the hexagonal cell model leads to slightly smaller SCF for the same neighbouring fibers, which can be explained by the fact that more fibers in the hexagonal cell model share the redistributed loads, consistent with the conclusion with Blassiau et al. [26]. However, it deserves pointing out the progressive failure of matrix also accelerates the localized fiber damage to some extent, which was not considered in the work of Blassiau et al. [26]. Besides, the cohesive interface model for predicting the interface failure is more advantageous than the interface bonding technique. Thus, modeling the transition from the initially bonded interface

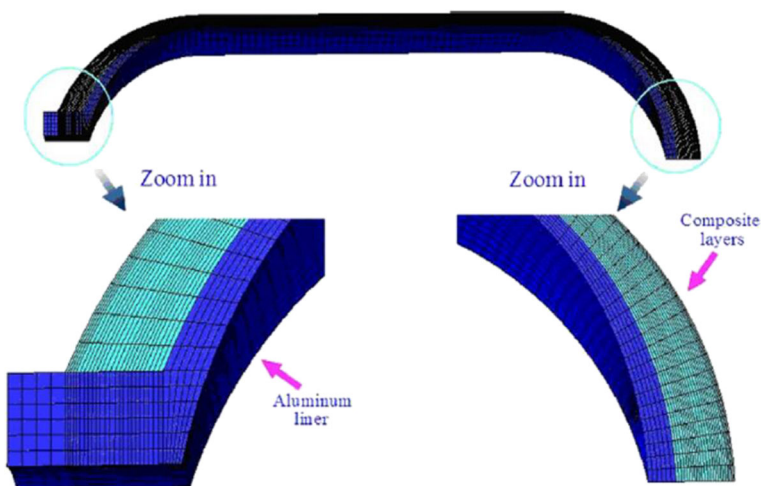
**Fig. 11** The finite element model for 74 L-capacity composite vessel

Table 3 Geometry parameters for the 74 L-capacity composite vessel

	Thickness (mm)	Wound angle (°)
Aluminum liner layer	5.0	--
First composite layer	2.1	90
Second composite layer	0.87	12.3
Third composite layer	0.87	15.4
Fourth composite layer	0.87	18.6
Fifth composite layer	2.1	90
Sixth composite layer	0.87	22
Seventh composite layer	0.87	27
Eighth composite layer	0.87	32
Ninth composite layer	0.6	38
Tenth composite layer	0.54	90

to debonded interface is significant to describe the load transfer and damage evolution of composites in this work, different from the work of Xia et al. [13, 20].

Figure 9 shows the tensile experiments and fracture specimens of carbon fiber/epoxy composites and Fig. 10 shows the tensile stress-strain curves of composites by FEA and experiments for four composite specimens. Based on the shear-lag model and Weibull distribution, the expression for the ultimate tensile strength (UTS) σ_u is given as [13, 14, 17, 18, 20]

$$\sigma_u = f\sigma_c \left(\frac{2}{m+2}\right)^{1/(m+1)} \left(\frac{m+1}{m+2}\right) + (1-f)\sigma_m, \quad \sigma_c = \left[\frac{\sigma_0^m \tau L_0}{r_f}\right] \quad (14)$$

where τ is the frictional shear stress at the debonded interface.

The UTS of composites by analytical solutions, FEA and experiments are listed in Table 2. By comparison, the UTS obtained by FEA is smaller than the experimental results. Besides, the UTS predicted using the analytical model approaches the experimental UTS when the interface sliding stress becomes large. They considered the initially debonded interface due to high residual stresses, and the interface slips against each other obeying the Coulomb friction law. However, the loading sharing model is required to highlight the effect of high SCF on the UTS when the interface stress τ becomes large. In contrast, the present FEA considered an initially perfect interface and subsequent interface crack initiation and propagation. Thus, the interface stress transfer and stress concentration effect are more accurately described.

Finally, the stress-strain tensile curve of carbon fiber/epoxy composites by FEA is further applied to the progressive failure analysis of composite pressure vessel. Since the Young’s modulus and tensile strength in the fiber principal direction dominate the burst strength of composite vessel, the tensile curve is taken as the longitudinal direction. Figure 11 shows the finite element model of composite vessel with 74 L capacity, which includes one 30° inner aluminum layer and ten 30° outer composite layers. The mesh

Table 4 Mechanical parameters of 6061 Al liner and carbon fiber/epoxy composites

	E_1 (GPa)	E_2 (GPa)	E_3 (GPa)	ν_{12}	ν_{23}	ν_{13}	G_{12} (GPa)	G_{23} (GPa)	G_{13} (GPa)
6061Al	70	70	70	0.3	0.3	0.3	27	27	27
Composite	120	11.41	11.41	0.33	0.49	0.33	7.92	3.792	7.92

E is the Young’s modulus, ν is the Poisson’s ratio and G is the shear modulus

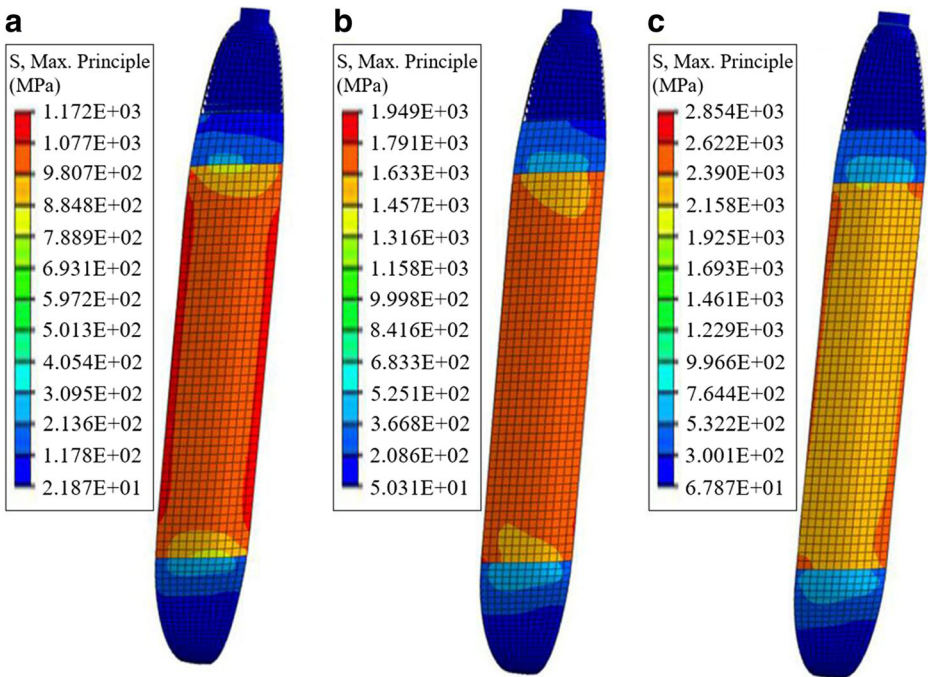


Fig. 12 The maximum principal stresses of composite vessel in the fiber principal direction at internal pressure (a) 40 MPa, (b) 60 MPa and (c) 80 MPa respectively

model includes 38,958 elements. Table 3 lists the winding geometry parameters and Table 4 shows the material parameters. The inner radius for cylinder is 183 mm. Figure 12 shows the fiber principal stresses at different internal pressure. Figure 13 shows the burst specimen of composite vessel. The burst pressure for composite vessel by FEA is about 90 MPa, close to the experimental result 94 MPa.

Fig. 13 Burst specimen of 74 L–capacity composite vessel specimen [25]



4 Conclusions

Based on the microscopic structures of carbon fiber/epoxy composites, this paper develops a large-scale finite element model with the hexagonal cell to study the progressive failure properties of composites. Different from most of existing works including Xia et al. [13, 20] and Blassiau et al. [26], all failure modes including fiber breakage, matrix damage evolution and interface debonding are considered in this work, where Monte Carlo simulation is used for fiber breakage, damage mechanics method is used for matrix damage and cohesive model is used for interface debonding. We originally develop a restart analysis-based finite element technique to predict all real-time progressive failure properties of micromechanical RVE.

From FEA, the following conclusions are obtained:

- (1) Relatively small thermal residual stress due to curing appears mainly at the matrix, which also affects the initial interface debonding to some extent.
- (2) During the early stage, rapidly increased matrix cracking and interface debonding are dominating failure modes that leads to severe stiffness degradation. During the later stage, few fiber breakage and fiber pullout appear, marking the collapse of structures.
- (3) The LLS model predicts the stress concentration on the second neighbouring fibers around the broken fiber accurately, but overestimates that on the first neighbouring fibers because it still neglects many factors including the matrix damage evolution and the initiation and propagation of interface crack. In addition, the hexagonal cell model as a more precise model leads to slightly smaller stress concentration for the same fibers around the broken fiber than the square cell model. Finally, the composite tensile strength predicted using the shear-lag model is consistent with the experimental result only when the frictional shear stress is large.

Acknowledgements Dr. P. F. Liu would sincerely like to thank the support by the National Key Fundamental Research and Development Project of China (No. 2015CB057603), the National Natural Science Funding of China (No. 51375435), the Open Project of State Key Laboratory of Mechanics and Control of Mechanical Structures of Nanjing University of Aeronautics and Astronautics of China (No. MCMS-0216G01) and the Open Project of State Key Laboratory for Strength and Vibration of Mechanical Structures of Xi'an Jiaotong University of China (No. SV2015-KF-09).

References

1. LLorca, J., Gonzalez, C., Molina-Aldareguia, J.M., Segurado, J., Seltzer, R., Sket, F., Rodriguez, M., Sádaba, S., Muñoz, R., Canal, L.P.: Multiscale modeling of composite materials: A roadmap towards virtual testing. *Adv. Mater.* **23**, 5130–5147 (2011)
2. Hedgepeth, J.M., Van Dyke, P.: Local stress concentrations in imperfect filamentary composite materials. *J. Compos. Mater.* **1**, 294–309 (1967)
3. Beyerlein, I.J., Landis, C.M.: Shear-lag model for failure simulations of unidirectional fiber composites including matrix stiffness. *Mech. Mater.* **31**, 331–350 (1999)
4. Nairn, J.A., Mendels, D.A.: On the use of planar shear-lag methods for stress-transfer analysis of multilayered composites. *Mech. Mater.* **33**, 335–362 (2001)
5. Mahesh, S., Hanan, J.C., Üstündag, E.E., Beyerlein, I.J.: Shear-lag model for a single fiber metal matrix composite with an elasto-plastic matrix and a slipping interface. *Int. J. Solids Struct.* **41**, 4197–4218 (2004)
6. Okabe, T., Takeda, N.: Elastoplastic shear-lag analysis of single-fiber composites and strength prediction of unidirectional multi-fiber composites. *Compos. Part A-Appl.* **33**, 1327–1335 (2002)

7. Landis, C.M., McMeeking, R.M.: A shear-lag model for a broken fiber embedded in a composite with a ductile matrix. *Compos. Sci. Technol.* **59**, 447–457 (1999)
8. Chen, Z.R., Yan, W.Y.: A shear-lag model with a cohesive fibre-matrix interface for analysis of fibre pull-out. *Mech. Mater.* **91**, 119–135 (2015)
9. Pimenta, S., Robinson, P.: An analytical shear-lag model for composites with 'brick-and-mortar' architecture considering non-linear matrix response and failure. *Compos. Sci. Technol.* **104**, 111–124 (2014)
10. Tsai, K.H., Kim, K.S.: The micromechanics of fiber pull-out. *J. Mech. Phys. Solids.* **44**, 1147–1159 (1996)
11. Sakai, M., Matsuyama, R., Miyajima, T.: The pull-out and failure of a fiber bundle in a carbon fiber reinforced carbon matrix composite. *Carbon.* **38**, 2123–2131 (2000)
12. Curtin, W.A.: Fiber pull-out and strain localization in ceramic matrix composites. *J. Mech. Phys. Solids.* **41**, 35–53 (1993)
13. Xia, Z., Curtin, W.A., Okabe, T.: Green's function vs. Shear-lag models of damage and failure in fiber composites. *Compos. Sci. Technol.* **62**, 1279–1288 (2002)
14. Zhou, S.J., Curtin, W.A.: Failure of fiber composites—a lattice green-function model. *Acta Mater.* **43**, 3093–3104 (1995)
15. Beyerlein, I.J., Phoenix, S.L.: Stress concentrations around multiple fiber breaks in an elastic matrix with local yielding or debonding using quadratic influence superposition. *J. Mech. Phys. Solids.* **44**, 1997–2039 (1996)
16. Landis, C.M., McMeeking, R.M.: Stress concentrations in composites with interface sliding, matrix stiffness and uneven fiber spacing using shear lag theory. *Int. J. Solids Struct.* **36**, 4333–4361 (1999)
17. Rajan, V.P., Curtin, W.A.: Micromechanical design of hierarchical composites using global load sharing theory. *J. Mech. Phys. Solids.* **90**, 1–17 (2016)
18. Ibnabdeljalil, M., Curtin, W.A.: Strength and reliability of fiber-reinforced composites: Localized load-sharing and associated size effects. *Int. J. Solids Struct.* **34**, 2649–2668 (1997)
19. Landis, C.M., Beyerlein, I.J., McMeeking, R.M.: Micromechanical simulation of the failure of fiber reinforced composites. *J. Mech. Phys. Solids.* **48**, 621–648 (2000)
20. Xia, Z., Okabe, T., Curtin, W.A.: Shear-lag versus finite element models for stress transfer in fiber-reinforced composites. *Compos. Sci. Technol.* **62**, 1141–1149 (2002)
21. Liu, P.F., Zheng, J.Y.: A Monte Carlo finite element simulation of damage and failure in SiC/Ti-Al composites. *Mat. Sci. Eng. A-Struct.* **425**, 260–267 (2006)
22. Cheng, T.L., Qiao, R., Xia, Y.M.: A Monte Carlo simulation of damage and failure process with crack saturation for unidirectional fiber reinforced ceramic composites. *Compos. Sci. Technol.* **64**, 2251–2260 (2004)
23. Gonza'lez, C., LLorca, J.: Mechanical behavior of unidirectional fiber-reinforced polymers under transverse compression: Microscopic mechanisms and modeling. *Compos. Sci. Technol.* **67**, 2795–2806 (2007)
24. Totry, E., Gonza'lez, C., LLorca, J.: Failure locus of fiber-reinforced composites under transverse compression and out-of-plane shear. *Compos. Sci. Technol.* **68**, 829–839 (2008)
25. Liu, P.F., Chu, J.K., Hou, S.J., Zheng, J.Y.: Micromechanical damage modeling and multiscale progressive failure analysis of composite pressure vessel. *Comput. Mater. Sci.* **60**, 137–148 (2012)
26. Blassiau, S., Thionnet, A., Bunsell, A.R.: Micromechanisms of load transfer in a unidirectional carbon fibre-reinforced epoxy composite due to fibre failures. Part 1: Micromechanisms and 3D analysis of load transfer: The elastic case. *Compos. Struct.* **74**, 303–318 (2006)
27. Xu, X.P., Needleman, A.: Numerical simulations of fast crack-growth in brittle solids. *J. Mech. Phys. Solids.* **42**, 1397–1434 (1994)
28. Li, L.B.: Micromechanical Modeling for Tensile Behaviour of Carbon Fiber - Reinforced Ceramic - Matrix Composites. *Appl. Compos. Mater.* **22**, 773–790 (2015)
29. Zhou, Y.X., Wang, Y., Xia, Y.M., Jeelani, S.: Tensile behavior of carbon fiber bundles at different strain rates. *Mater. Lett.* **64**, 246–248 (2010)
30. Ha, S.K., Jin, K.K., Huang, Y.: Micro-mechanics of failure (MMF) for continuous fiber reinforced composites. *J. Compos. Mater.* **42**, 1873–1895 (2008)
31. Lemaitre, J., Desmorat, R.: *Engineering damage mechanics*. Springer, Berlin (2005)
32. Hori, M., Nemat-Nasser, S.: On two micromechanics theories for determining micro-macro relations in heterogeneous solids. *Mech. Mater.* **31**, 667–682 (1999)
33. Tan, H., Huang, Y., Liu, C., Geubelle, P.H.: The Mori-Tanaka method for composite materials with nonlinear interface debonding. *Int. J. Plast.* **21**, 1890–1918 (2005)
34. Zhang, Y.F., Xia, Z.H., Ellyin, F.: Evolution and influence of residual stresses/strains of fiber reinforced laminates. *Compos. Sci. Technol.* **64**, 1613–1621 (2004)
35. Xia, Z.H., Zhou, C.W., Yong, Q.L., Wang, X.W.: On selection of repeated unit cell model and application of unified periodic boundary conditions in micro-mechanical analysis of composites. *Int. J. Solids Struct.* **43**, 266–278 (2006)